

# FAST MEASUREMENTS OF THE ELECTRON BEAM TRANSVERSE SIZE AND POSITION ON SOLEIL STORAGE RING

M. Labat\*, A. Bence, N. Hubert, D. Pédeau, Synchrotron SOLEIL, Gif-sur-Yvette, France  
 M. M. Patil, M. Caselle, A. Ebersoldt, E. Bründermann,  
 Karlsruhe Institute of Technology, Karlsruhe, Germany

## Abstract

On SOLEIL storage ring, three beamlines are dedicated to electron beam diagnostics: two in the X-ray range and one in the visible range. The visible range beamline uses the synchrotron radiation which is emitted in one of the ring dipoles and further extracted by a slotted mirror operated in surf-mode (surfing on the upper part of the synchrotron layer). The radiation in the visible range is then transported towards a diagnostic hutch in the experimental hall, allowing electron beam imaging at the source point onto a standard CCD camera. In the perspective of prototyping works for the eventually forthcoming upgrade of SOLEIL, and for the on-going commissioning of a new Multipole Injection Kicker (MIK), we recently installed in this hutch two new branches ended by two new cameras (a KALYPSO system and a standard CMOS camera). We report in this paper the first results obtained on those branches.

## INTRODUCTION

SOLEIL storage ring presently delivers synchrotron radiation to 29 beamlines. The stability of the delivered photon beams, a main figure of merit for users, relies on an accurate monitoring of the electron beam orbit and electron beam size / emittance at users source points. The electron beam size / emittance is measured independently by two pinhole camera (PHC) systems, located at two different places of the ring. One of the PHC measurement is used in a feedback loop to maintain the vertical emittance within  $\pm 5\%$ . However, with typical exposure times of 50–100 ms, those systems cannot follow fast beam dynamics features at the turn-by-turn scale for instance.

The installation of a new injection magnet and the perspective of an upgrade for SOLEIL recently revealed the need for an additional beam size diagnostic with a faster response.

We therefore decided to upgrade our visible range MRSV (*Moniteur de Rayonnement Synchrotron Visible*) beamline with two new branches. This work presents the preliminary results obtained on those branches.

## EXPERIMENTAL SETUP

The experimental layout of the MRSV beamline is presented in Fig. 1. The synchrotron radiation of one of the ring dipoles (ANS-C01) is extracted using a slotted mirror operated in *surf-insertion* mode: the mirror is surfing on top of the synchrotron radiation layer to catch visible range

photons. Because of heat load issues, we can't operate the mirror in *slot-insertion* mode, i.e. centered on the beam axis with synchrotron radiation X-rays going through the slot, at high current. The synchrotron radiation is then transported via a set of mirrors down to a hutch in the experimental hall. On the beam path inside the tunnel are successively placed: a motorized slit to define the horizontal collection angle  $\theta_x$  of the beamline and a spherical lens for refocussing. At the arrival on the optical bench in the hutch, the synchrotron radiation is splitted into several branches.

Initially, three branches were implemented (see pink boxes in Fig. 1): one with a fast diode for filling pattern measurement, one with a Streak Camera for bunch length measurement and one with a standard ethernet camera for a coarse imaging of the beam at the source point. We added two new branches to test higher resolution / higher speed imaging systems for beam size retrieval.

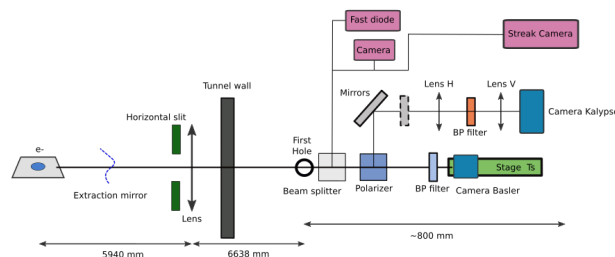


Figure 1: Layout of the MRSV beamline with its three initial branches in pink, and its two new branches.

## BEAMLINE MODELING

To achieve an accurate imaging, an accurate modeling of the beamline is mandatory. We used for that the SRW (*Synchrotron Radiation Workshop*) code [1]. In Fig. 2 is first presented the simulated effect of using the extraction mirror in *surf* rather than in *full* (or *slot*) –insertion mode. Because of the dissymmetry of the extraction, there is nearly no more difference between the polarization components of the radiation.

After a first attempt of comparison between measured and simulated intensity distributions in the image plane of the MRSV beamline, we realized that the beamline was suffering from strong stigmatism: the image plane in  $y$  was few tens of centimeters downstream the image plane in  $x$ . Because the focussing lens in the tunnel is spherical, we immediately suspected the extraction mirror to introduce this stigmatism. To verify this interpretation, we simulated the effect of a

\* marie.labat@synchrotron-soleil.fr

Content from this work may be used under the terms of the CC BY 3.0 licence (© 2021). Any distribution of this work must maintain attribution to the author(s), title of the work, publisher, and DOI

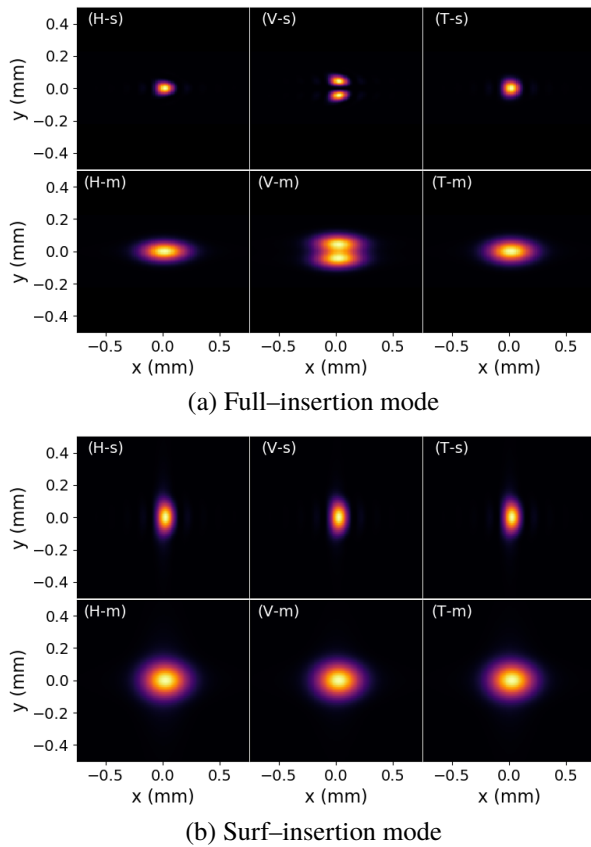


Figure 2: Intensity distribution in the image plane simulated with SRW using an extraction mirror in (a) full-insertion and (b) surf-insertion mode. Polarization is (left) Horizontal, (middle) Vertical and (Right) Total, using (top line) single-electron, (bottom line) multi-electron mode. Other parameters:  $\lambda=400$  nm,  $f_{xy}=3.21$  m,  $D=6.984$  m,  $\theta_x=3.5$  mrad,  $\theta_y=10$  mrad.

double focussing: an astigmatic one from the spherical lens together with a stigmatic one (only along vertical dimension) from the extraction mirror. The result is an effective focal length  $f_x$  along  $x$  and  $f_y$  along  $y$  where  $f_x \neq f_y$ . Fitting the experimental observations of the intensity distributions versus  $D$  the distance from lens to camera for several wavelengths led to  $f_x=3.21$  m and  $f_y=3.4$  m at 400 nm. The good agreement between model and simulation confirmed that under heat load, the extraction mirror becomes slightly convex in the  $y$  direction, introducing an additional focussing in this direction. In Fig. 3 is presented the result of the simulated effect of this stigmatic focussing on the beam distribution in the  $x$  image plane. The image distribution is further distorted along  $y$ .

In Fig. 4, we finally present the simulated and measured effect of the distance  $D$  from lens to camera for a wide horizontal collection angle  $\theta_x$ . Even though images are displayed in logarithmic scale, the agreement between simulation and experiment remains reasonable.

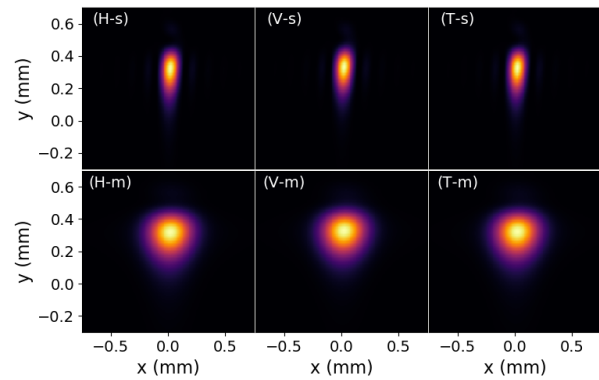


Figure 3: Intensity distribution in the image plane simulated with SRW using an extraction mirror in surf-insertion mode with  $f_x=3.21$  m and  $f_y=3.4$  m. Other parameters as in Fig. 2.

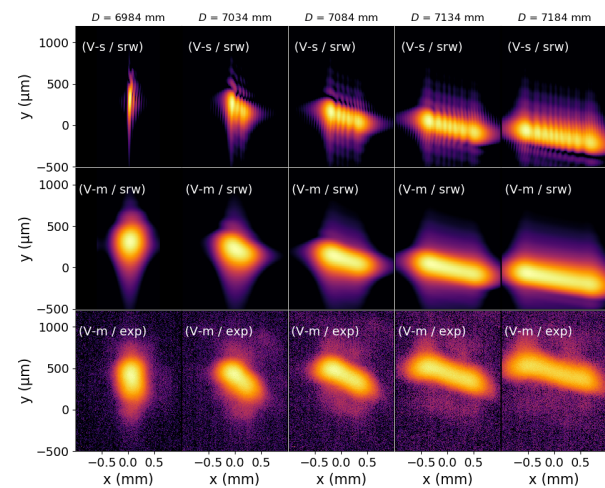


Figure 4: Intensity distribution in the image plane simulated with SRW (first line in single-electron, second line in multi-electron mode) and experimentally measured (third line) versus  $D$ . Extraction mirror in surf-insertion mode with  $f_x=3.21$  m and  $f_y=3.4$  m,  $\theta_x=\theta_y=10$  mrad,  $\lambda=400$  nm, vertical polarization. Images in logarithmic scale. Camera for experiment: Basler ace1920.

## FIRST NEW BRANCH: NB#1

Confident in the modeling of the beamline, we then used SRW simulations to optimize the distance  $D$ , the observation wavelength  $\lambda$  and the horizontal collection angle  $\theta_x$  to get the highest contrast between the single-electron spot size (PSF) and the multi-electron spot size. The higher indeed will be this contrast, the more sensitive should be the final beam size measurement. The best result was obtained at the shortest reachable wavelength (400 nm) with the maximum collection angle (10 mrad) in the  $x$  image plane. We implemented the first new branch NB#1 accordingly. The radiation is spectrally filtered using a bandpass filter centered at 400 nm with 10 nm bandwidth, for the sake of simplicity the vertically polarized component is retained using a polarizing beamsplitter cube (see Fig. 1), while an ace1920

CMOS camera from Basler is used to record the images with a  $5.6 \mu\text{m}$  pixel pitch.

We then investigated on the beam size retrieval method from the experimental images. For nearly Gaussian PSF profiles, beam size retrieval can simply be achieved by fitting the beam profiles in the image plane with Gaussian functions, and then quadratically subtract the widths of the PSF to those fitted widths. But in our case of imaging with a surf-inserted mirror, a chromatic focussing and a large horizontal collection angle, the PSF functions are far from being Gaussian. We therefore tried, as a first step, to fit the beam profiles in the image plane with the convolution of the SRW simulated PSFs with Gaussian functions of width  $S_x$ ,  $S_y$ . ( $S_x$ ,  $S_y$  would correspond to the *real* beam size in the image plane, i.e. beam size at source point  $\sigma_x$ ,  $\sigma_y$  magnified by  $M$  the beamline magnification). The results were not satisfactory in the  $y$  direction because images are recorded in the  $x$  image plane, not in the  $y$  plane. We then tried to compute a pseudo-PSF for the  $y$  plane, making the deconvolution of the SRW simulated beam profile with a Gaussian function of width  $S_y = M \times \sigma_y$ , where  $\sigma_y$  is the beam vertical size at source point used as input in the simulation. However, this method was still leading to beam size at the source point several times larger than the expected one. This was essentially due to the fact that we could not reach a perfect agreement between SRW simulation and measurement of the beam distribution in the image plane probably because of complicated mirror surface distortions. We finally tried to convolute the previous pseudo-PSF with a Gaussian error function. The width of this function was manually adjusted to match the beam size retrieved with the beam size expected. Beam size retrieval with this method is illustrated in Fig. 5. Up to now, this is the best method we could set.

In order to test the sensitivity of our measurement, we then simultaneously recorded the vertical beam sizes measured on NB#1, PHC#1 and PHC#3 as a function of the vertical emittance. The results are shown in Fig. 6. This measurement first reveal the high level of fluctuation on NB#1 (more than 100% fluctuation in the beam size measurement). While the exposure time for PHCs is in the 50–100 ms range, the exposure time on NB#1 is  $30 \mu\text{s}$ , i.e. nearly three orders of magnitude, so we expected of course more fluctuations on NB#1. But the main source of fluctuation is most probably due to the radiation transport in air, over more than 10 meters and passing via differently air conditioned areas. The amplitude of the fluctuations is indeed far above the possible *physical* ones, of the order of a few microns.

## SECOND NEW BRANCH: NB#2

The polarizer at the entrance of the optical bench splits the synchrotron radiation in one vertically polarized component going straight to NB#1, and one horizontally polarized component deflected by 90 degrees. This component of the synchrotron radiation is the one used for our second branch NB#2. The radiation on NB#2 is transported with mirrors down to a Kalypso camera [2]. This camera was provided

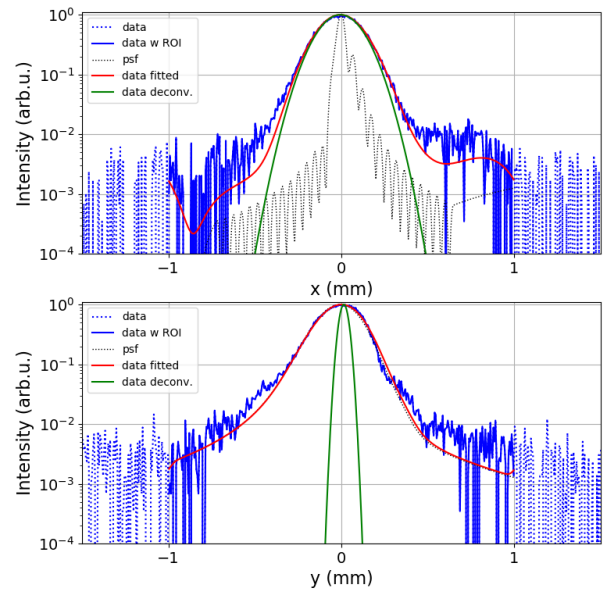


Figure 5: Example of beam size retrieval from measured images. (data) experimental profiles corresponding to line cuts of 2 pixels at maximum intensity location. (data w roi) data restricted to a ROI of  $\pm 1$  mm. (psf) Point Spread Function simulated with SRW and eventually corrected. (data fitted) Experimental profiles restricted to ROI fitted by convolution of a Gaussian profile with the PSF function. (data deconv.) Gaussian profile obtained from fit.  $D=6.994$  m,  $\theta_x=\theta_y=10$  mrad,  $\lambda=400$  nm, polarization is vertical.

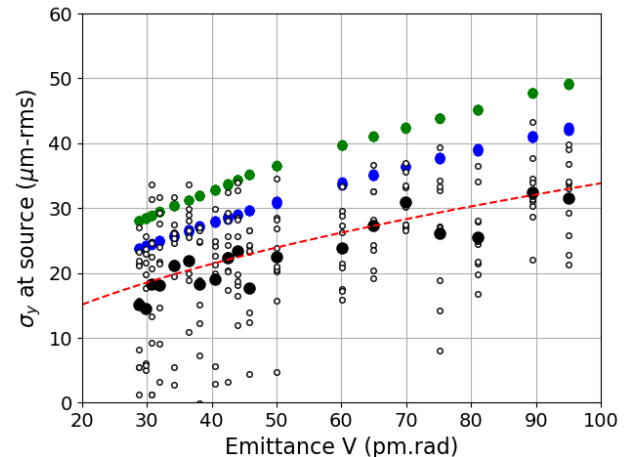
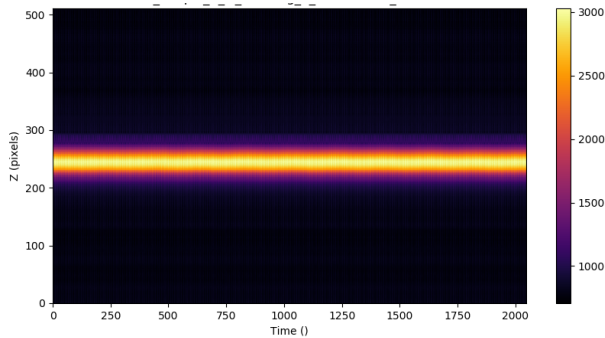


Figure 6: Vertical beam size measured versus vertical emittance by (green dot) PHC#1, (blue dot) PHC#3, (o) MRSV HR branch single shot, (●) MRSV HR branch average of the 10 single shots.  $D=6.994$  m,  $\theta_x=\theta_y=10$  mrad,  $\lambda=400$  nm, polarization is vertical.

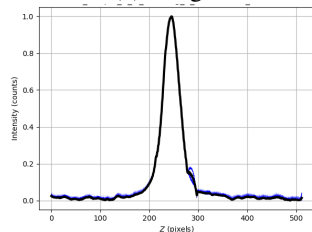
by KIT. It consists of a linear array detector with an ultra-fast reading electronics. This system is described in details in [2]. To match the linear array geometry, the photon beam is refocussed with a pair of cylindrical lenses ( $f=100$  mm). To obtain a reasonable resolution with the maximum flux, a bandpass filter of 80 nm bandwidth centered at 600 nm is used.

Content from this work may be used under the terms of the CC BY 3.0 licence (© 2021). Any distribution of this work must maintain attribution to the author(s), title of the work, publisher, and DOI

A typical example of a Kalypso image is presented in Fig. 7(a). Each vertical line of the image corresponds to one record of the light distribution along the linear array. In the example, it is the vertical distribution of the beam which is captured. Along the image horizontal axis are displayed the successive records. Each record can be externally or internally triggered up to 3 MHz which offers outstanding opportunities for machine physics studies. In the example, the records were triggered by the turn-by-turn clock (846 kHz), so that each record corresponds to the imaging of the same portion of the bunch train turn after turn.



(a) Image



(b) Normalized vertical intensity profile

Figure 7: (a) Example of a Kalypso camera image in users operation at 500 mA. (b) Normalized projection of the (a) image along the horizontal axis to provide with the beam distribution along the vertical axis.

The Kalypso system is still under commissioning on NB#2. But we could already perform an interesting machine physics experiment. We used indeed the Kalypso camera to follow the effect of the injection on the stored beam during the operation of SOLEIL. To maintain a constant current, top-up injection is performed into the storage ring. Every few minutes, 4 kickers are used to create a bump on the stored beam orbit, allowing the injection of few additional mA. Because the bump is not perfectly closed, we can observe on the beam position monitors a transient displacement of the beam in both the horizontal and the vertical planes. Launching the acquisition of the Kalypso camera slightly before the injection time, and using an external turn-by-turn trigger, we could record the images presented in Fig. 8. The top image shows the horizontal beam distribution and the bottom image shows the vertical beam distribution. We can change the imaging plane using a crossed or non-crossed periscope on the photon beam path. In both planes, we clearly observe the kick given at the injection time, but we can also follow

the evolution of the beam back to its equilibrium on a real turn-by-turn basis. The beam oscillates as expected in both planes at the synchrotron frequency with a damping time significantly shorter in the vertical than in the horizontal plane.

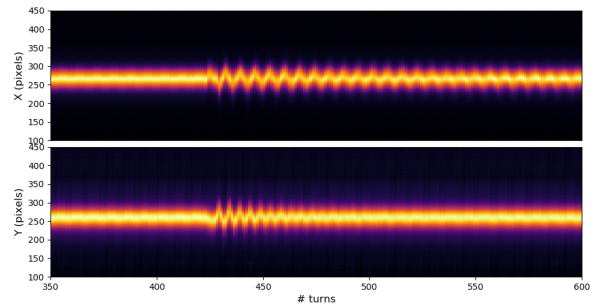


Figure 8: Kalypso images recorded on MRSV beamline. Recording launched a few hundred turns before injection time. Imaging of (Top) the horizontal and (bottom) the vertical distribution of the beam.

## CONCLUSION

We presented here recent results obtained on the two new branches NB#1 and 2 of our visible range MRSV beamline.

We made significant efforts to obtain a satisfactory modeling of our beamline relying on SRW simulations. We managed to include the effect of the surf-insertion mode and of a stigmatic focussing induced by the mirror. Unfortunately, some discrepancies remain between simulation and measurement, so that up to now, we can only retrieve the beam sizes at the source point including, in addition to the PSF, an additional arbitrary –but constant– contribution to the beam size. Next January, the extraction system for the MRSV beamline will be upgraded (new extraction mirror and new cooling system). This should enable to improve the accuracy of the imaging on NB#1 in surf-insertion mode, but also to work in the slot-insertion mode in users operation.

The preliminary results obtained on NB#2 are very encouraging. The ultra-high repetition rate of the camera enabled already to follow the beam dynamics at injection in one single image. By the end of 2021, we plan to improve the focussing on the camera and to calibrate the magnification on NB#2 to have an absolute beam size measurement.

Both NB#1 and 2 strongly suffer from a very high level of fluctuations most probably due to the long in-air transport. We'll try to upgrade the beamline to move it under-vacuum along 2022.

## REFERENCES

- [1] O. Chubar, P. Elleaume, "Accurate and Efficient Computation of Synchrotron Radiation in the Near Field Region", in *Proc. 6th European Particle Accelerator Conf. (EPAC'98)*, Stockholm, Sweden, Jun. 1998, paper THP01G, p.1177-1179.
- [2] M. Caselle *et al.*, "Ultrafast linear array detector for real-time imaging", *Proc. of SPIE*, vol. 10937, 1093704-1, 2019.